PHYSICAL REVIEW A **81**, 032517 (2010)

Formation of fragment momentum correlations in three-body predissociation of triatomic hydrogen: The interplay of geometry-dependent nonadiabatic coupling and ground-state dynamics

U. Galster
MPIPKS, D-01187 Dresden, Germany

(Received 31 August 2009; published 29 March 2010)

Momentum correlations in three-body predissociation of triatomic hydrogen are investigated by quasiclassical trajectory calculations. It is shown that nonadiabatic couplings that trigger predissociation of the $2sA_1'$ state of H_3 imprint their geometric properties on the momentum correlation structures observed after dissociation. A simple symmetry-based model of the geometric coupling properties succeeds in reproducing most of the experimentally observed patterns. The ground-state dynamics that transform the geometric properties of the coupling into the final momentum correlations are identified.

DOI: 10.1103/PhysRevA.81.032517 PACS number(s): 31.50.Gh, 31.15.xg, 34.80.Ht

I. INTRODUCTION

Predissociation of H_3 Rydberg states has attracted much interest over the past two decades [1–12]. There are two major reasons for the persistent attention to this subject. First, the understanding of the dissociation mechanisms is of crucial importance for determining the rate of dissociative recombination of H_3^+ in interstellar clouds, which is decisive for the production rate of various molecules [13–18]. Second, H_3 represents an ideal prototype for the in-depth study of the fundamental predissociation mechanisms of polyatomic molecules [1,2,10,19]. Electronically excited rovibronic levels of H_3 are quasibound and feature lifetimes which range between 200 fs and 700 ns [8,20–22]. They are predissociated by nonadiabatic transitions to one of the two Jahn-Teller coupled electronic ground states. The dissociation limits of the corresponding two ground-state potential sheets are three-body [$3\times$ H(1s)] breakup for the upper surface and two body ($H + H_2$) as well as three-body breakups in the case of the lower surface.

In general, nonadiabatic couplings which are involved in predissociation prefer transitions at specific nuclear geometries. These geometries are often manifestations of symmetry properties. In conjunction with geometric properties of the initial vibrational wave function, they determine initial nuclear wave functions for the dissociation on the ground-state surfaces.

Recent experimental observations indicate that the effects of such geometric properties are reflected in correlations among the momenta of the three H atoms emerging from three-body predissociation of state-selected H_3 [3,4,12,23]. The states of which three-body predissociation were investigated to date comprise several rovibrational levels of electronic states of H_3 as well as D_3, especially $2sA_1'$, $2pA_2''$, $3pE'$, $3sA_1'$, and $3dE''$.

The structures observed for the electronic states $2sA_1'$ and $2pA_2''$ are not only much simpler than those observed for the energetically higher states (e.g., those for the principal quantum number $n = 3$), but also show clear regularities. The reason is that for the levels of $2sA_1'$ and $2pA_2''$ the set of electronic states involved in the nonadiabatic coupling processes is reduced to the initial electronic state and the two ground states of H_3 only. Nonadiabatic coupling between $2sA_1'$ and $2pA_2''$ is prohibited by symmetry, due to the absence of nonadiabatic coupling operators which transform A_2'' into A_1' (radiative dipole coupling is allowed, but very inefficient due to the low-level separation). For the lower vibrational states studied here, higher electronic states are energetically inaccessible because all the rovibronic levels in question are separated by at least 0.6 eV from the lowest level of the higher electronic states.

Specific regularities appear among the momentum correlations observed after predissociation of the various vibrational levels of $2sA_1'$. Currently, there are two publications concerning the interpretation of these levels. Lepetit *et al.* [23] showed that the dominant structure of momentum configurations of the levels $2sA_1'$ $(v_2 = 0)$ can be explained by rovibronic symmetry conservation and geometric phase effects. Lehner and Jungen [24] succeeded in reproducing many features of $2sA_1'$ $(v_2 = 0)$ as well as $2sA_1'$ $(v_2 = 1)$ levels by using a semiclassical trajectory surface-hopping method.

This article also focuses on the interpretation of momentum correlations emerging from several vibrational levels ($v_1 = \{0, 1, 2\}$, $v_2 = \{0, 1\}$) of $2sA_1'$ for H_3 as well as for D_3. The aim is to give a clear physical picture of the structures appearing in the momentum correlations. It is shown that most of the structures can be understood and even reproduced by mere symmetry arguments and classical trajectory propagation.

The predissociation mechanism is described by a sequence of two steps: First the nonadiabatic transition to the two ground states and second the following propagation on the two ground-state potential surfaces. In both steps the nuclear wave function is subject to modifications. The first step is described in a model which uses symmetry properties of the initial rovibrational wave function and the coupling to define the initial vibrational wave function for step two. The second step is then carried out by using a classical trajectory Monte Carlo (CTMC) simulation.

The nonadiabatic coupling between $2sA_1'$ and the ground states is mediated by a vibronic interaction which involves derivative couplings in the coordinate space of the two degenerate modes. This space can be described by a set of polar coordinates (Q_r, φ). In the model of Lehner and Jungen, the coupling which is generated by the coodinate φ is considered.

The approach presented here differs from Lehner and Jungen's work in many aspects. In particular, we make two major advances: The nonadiabatic coupling from the $2sA_1'$ to the ground states involves both coordinates Q_r and φ; and the motion on the ground-state surfaces is initiated by a well-defined initial phase-space distribution given by the Wigner quasiprobability distribution. In Lehner and Jungen's work the initial conditions on each surface are derived from energy conservation as well as the gradient of the potential.

This article also provides additional insight into the time-dependent dissociation dynamics on the upper ground-state sheet, which elucidates the process of breakup pattern formation.

The present work does not include transitions (surface hopping) between the two ground states, as included in Lehner and Jungen's work. Thus the description presented here is restricted to the motion which remains in one of the two electronic ground states after the nonadiabatic transition. As a consequence, a few experimental features will not be reproduced by this model, which will be discussed later on.

This article is organized as follows: In Sec. II, a theoretical description of predissociation of $2sA_1'$ is discussed. A model for the nonadiabaic couplings is derived on the basis of symmetry considerations. Section III shows how this model is applied for a CTMC simulation. The main part of this publication is Sec. IV, which is concerned with the results of the quasiclassical simulations and their interpretation. A conclusion is given in Sec. V.

II. PREDISSOCIATION OF $2sA_1'$ LEVELS

Predissociation of the lower vibrational levels of the electronic state $2sA_1'$ of H_3 and D_3 proceeds by direct nonadiabatic transition to the Jahn-Teller coupled ground states followed by a propagation of the rovibrational part of the wave function on the ground-state surfaces. These surfaces form a conical intersection at the equilateral triangle geometry. In this section we describe the transition process in more detail and work out reasonable approximations to reproduce the essential features of the coupling between $2sA_1'$ and the ground states.

For simplicity, we first introduce a shorthand notation for the involved electronic basis states

$$\begin{aligned} \mathbf{e}_{2s} &\equiv |\phi_{2s}(\mathbf{Q})\rangle, \\ \mathbf{e}_u &\equiv |\phi_u(\mathbf{Q})\rangle, \\ \mathbf{e}_l &\equiv |\phi_l(\mathbf{Q})\rangle, \end{aligned} \tag{1}$$

where $|\phi_{2s}(\mathbf{Q})\rangle$ refers to the initial state $2sA_1'$ and $|\phi_l(\mathbf{Q})\rangle$, $|\phi_u(\mathbf{Q})\rangle$ refer to the lower and upper adiabatic ground states, respectively. Using this basis set, the Hamiltonian describing the nuclear motion is given by

$$\mathbf{H} = T_N \mathbf{I} + \begin{pmatrix} V_i & \Lambda_{2s,u} & \Lambda_{2s,l} \\ \Lambda_{2s,u} & V_u & \Lambda_{u,l} \\ \Lambda_{2s,l} & \Lambda_{u,l} & V_l \end{pmatrix}. \tag{2}$$

Here T_N denotes the kinetic-energy operator for the nuclei, $\mathbf{I}$ the identity matrix, and V_{2s}, V_u, and V_l the adiabatic potentials (including diagonal corrections). $\Lambda_{2s,u}$, $\Lambda_{2s,l}$, and $\Lambda_{u,l}$ describe the nonadiabatic couplings. As $\mathbf{H}$ is time independent, the temporal evolution of the rovibronic wave function Ψ^{evr} of a predissociating level of $2sA_1'$ is given by

$$|\Psi^{\text{evr}}(t)\rangle = \exp\left[-i\mathbf{H}t\right] \chi_{2s}(0)\mathbf{e}_{2s}, \tag{3}$$

where $\chi_{2s}(0)$ denotes the initial rovibrational wave function of the electronically excited state. The time evolution will result in a population transfer into the ground states over times which correspond to the natural lifetime ($\tau \approx 200$ fs [20]) of $2sA_1'$. However, the dissociation on both of the ground-state sheets proceeds within ≈ 20 fs [25]. Thus, fractions of $\chi_{2s}(t)$ transferred to the ground state will rapidly propagate away from the equilibrium geometry and will be inhibited from further interaction with $2sA_1'$. For this reason, we can simplify the description as follows: We consider the fraction of the population which is transferred to one of the ground states over a small time interval $[t', t' + dt']$. This fraction is given by

$$\begin{aligned} d\left|\Psi_{u,l}^{\text{evr}}(t')\right\rangle &= -i\mathbf{P}_{u,l}\mathbf{H}\chi_{2s}(t')\mathbf{e}_{2s}dt' \\ &= -i[\Lambda_{2s,u}\chi_{2s}(t')\mathbf{e}_u + \Lambda_{2s,l}\chi_{2s}(t')\mathbf{e}_l]dt', \end{aligned} \tag{4}$$

where $\mathbf{P}_{u,l}$ is the projection on the the subspace spanned by $\mathbf{e}_u$ and $\mathbf{e}_l$. As no significant population is transferred back into $2sA_1'$, this results in an exponential decrease of the population of the excited state

$$\chi_{2s}(t) = \chi_{2s}(0) \exp\left[-iEt - \frac{t}{\tau}\right], \tag{5}$$

where E is the rovibrational energy and τ the lifetime of $2sA_1'$. Neglecting the coupling back to the excited state, the evolution of $d|\Psi_{u,l}^{\text{evr}}(t')\rangle$ on the coupled ground-state surfaces for $t > t'$ is described by

$$d\left|\Psi_{u,l}^{\text{evr}}(t)\right\rangle = \exp[-i\mathbf{H}_{u,l}(t-t')]d\left|\Psi_{u,l}^{\text{evr}}(t')\right\rangle, \tag{6}$$

where $\mathbf{H}_{u,l} = \mathbf{P}_{u,l}\mathbf{H}\mathbf{P}_{u,l}$. Inserting Eq. (4) into Eq. (6) and integrating over t' results in

$$\begin{aligned} \left|\Psi_{u,l}^{\text{evr}}(t)\right\rangle = -i \int_0^t &\exp[-i\mathbf{H}_{u,l}(t-t')][\Lambda_{2s,u}\chi_{2s}(t')\mathbf{e}_u \\ &+ \Lambda_{2s,l}\chi_{2s}(t')\mathbf{e}_l]dt'. \end{aligned} \tag{7}$$

In a simplified way, this equation can be interpreted as follows: In a small time interval dt', the fraction $[\Lambda_{2s,u}\chi_{2s}(t')\mathbf{e}_u + \Lambda_{2s,l}\chi_{2s}(t')\mathbf{e}_l]dt'$ leaks from the population of the excited state into the continuum. Thereby each fraction is modified by the action of the coupling operators $\Lambda_{2s,u}$ and $\Lambda_{2s,l}$. These fractions then evolve on the two coupled ground-state surfaces, which is described by the term $\exp[-i\mathbf{H}_{u,l}(t-t')]$. At time t many fractions are accumulated in the ground state and the total wave function $|\Psi_{u,l}^{\text{evr}}(t)\rangle$ is obtained by summing up these fractions, which is expressed by the integral in Eq. (7).

According to symmetry arguments [20], $2sA_1'$ can only be coupled by a vibronic interaction with the degenerate modes. The corresponding nonadiabatic coupling terms are

$$\Lambda_{2s,u/l} = \left[\langle\phi_{2s}|\frac{\partial}{\partial Q_{2a}}|\phi_{u/l}\rangle\frac{\partial}{\partial Q_{2a}} + \langle\phi_{2s}|\frac{\partial}{\partial Q_{2b}}|\phi_{u/l}\rangle\frac{\partial}{\partial Q_{2b}}\right], \tag{8}$$

where Q_{2a} and Q_{2b} are the normal coordinates of the degenerate modes. In this notation, the subscript u/l denotes either an index u or an index l for the whole equation, respectively. After

TABLE I. Characters of the one-dimensional irreducible representations of the double group of S_3.

	$\hat{\sigma}_1$	$\hat{C}^+$	I_R	
A_1	1	1	1	$\phi_{2s}, \frac{\partial}{\partial Q_r}$
A_2	−1	1	1	$\frac{\partial}{\partial \varphi}$
$\bar{A}_1$	1	1	−1	$\phi_l, \mathcal{A}_l, \mathcal{B}_u$
$\bar{A}_2$	−1	1	−1	$\phi_u, \mathcal{A}_u, \mathcal{B}_l$

a transformation to polar coordinates (Q_r, φ) [see Appendix, Eq. (A6)], this becomes

$$\Lambda_{2s,u/l} = \left[\langle \phi_{2s} | \frac{\partial}{\partial Q_r} | \phi_{u/l} \rangle \frac{\partial}{\partial Q_r} + \langle \phi_{2s} | \frac{\partial}{\partial \varphi} | \phi_{u/l} \rangle \frac{1}{Q_r^2} \frac{\partial}{\partial \varphi} \right]. \tag{9}$$

The terms $\langle \phi_{2s} | \frac{\partial}{\partial Q_r} | \phi_{u/l} \rangle$ and $\langle \phi_{2s} | \frac{\partial}{\partial \varphi} | \phi_{u/l} \rangle$ represent integrals over the electronic coordinate space and are functions of the nuclear coordinates

$$\begin{aligned} \mathcal{A}_{u/l}(Q_1, Q_r, \varphi) &\equiv \langle \phi_{2s} | \frac{\partial}{\partial Q_r} | \phi_{u/l} \rangle, \\ \mathcal{B}_{u/l}(Q_1, Q_r, \varphi) &\equiv \langle \phi_{2s} | \frac{\partial}{\partial \varphi} | \phi_{u/l} \rangle. \end{aligned} \tag{10}$$

In the following, we derive approximate expressions for these functions. As we are interested in nonadiabatic transitions from the lower vibrational levels of the $2s\,A_1'$ state, the goal is to reproduce the essential features in the regions of nuclear coordinate space where the vibrational wave function has significant amplitude. This region is limited to configurations which deviate from the equilibrium geometry by $\lesssim$25% of the binding distance.

First we analyze the symmetry of these functions. As both ϕ_u and ϕ_l feature a geometric phase (change of sign for $\varphi \to \varphi + 2\pi$), we use the double group of S_3 [26] to characterize the symmetry properties. This group is defined for the double-cover space for nuclear configurations. In this space, the range of the angle φ is extended to $[0, 4\pi]$ to facilitate the description of functions featuring a geometric phase [27]. The operation $I_R : (\varphi \to \varphi + 2\pi \bmod 4\pi)$ is an additional group element of the double group of S_3. It gives rise to two additional one-dimensional irreducible representations $\bar{A}_1$ and $\bar{A}_2$ (see Table I).

The function ϕ_{2s} and the operator $\frac{\partial}{\partial Q_r}$ are totally symmetric with respect to the double group of S_3. The operator $\frac{\partial}{\partial \varphi}$ transforms according to an A_2 irreducible representation, while the functions ϕ_u and ϕ_l have symmetries $\bar{A}_2$ and $\bar{A}_1$, respectively [23]. As a consequence, we find the following symmetries for the functions $\mathcal{A}_{u/l}$ and $\mathcal{B}_{u/l}$

$$\begin{aligned} \Gamma(\mathcal{A}_u) &= A_1 \otimes A_1 \otimes \bar{A}_2 = \bar{A}_2, \\ \Gamma(\mathcal{A}_l) &= A_1 \otimes A_1 \otimes \bar{A}_1 = \bar{A}_1, \\ \Gamma(\mathcal{B}_u) &= A_1 \otimes A_2 \otimes \bar{A}_2 = \bar{A}_1, \\ \Gamma(\mathcal{B}_l) &= A_1 \otimes A_2 \otimes \bar{A}_1 = \bar{A}_2. \end{aligned} \tag{11}$$

As the nuclear coordinates Q_1 and Q_r are not affected by symmetry operations, the symmetry of these functions is expressed by φ only. Complete basis sets for the functions of symmetries $\bar{A}_1$ and $\bar{A}_2$ are given by [28]

$$\begin{aligned} &\bar{A}_1 : \sin 3\left(n + \tfrac{1}{2}\right)\varphi \quad n = 0, 1, \ldots, \\ &\bar{A}_2 : \cos 3\left(n + \tfrac{1}{2}\right)\varphi \quad n = 0, 1, \ldots. \end{aligned} \tag{12}$$

Thus, the functions $\mathcal{A}_{u/l}$ and $\mathcal{B}_{u/l}$ can be written as

$$\begin{aligned} \mathcal{A}_u &= \sum_n a_u^{(n)}(Q_1, Q_r) \cos 3\left(n + \frac{1}{2}\right)\varphi, \\ \mathcal{A}_l &= \sum_n a_l^{(n)}(Q_1, Q_r) \sin 3\left(n + \frac{1}{2}\right)\varphi, \\ \mathcal{B}_u &= \sum_n b_u^{(n)}(Q_1, Q_r) \sin 3\left(n + \frac{1}{2}\right)\varphi, \\ \mathcal{B}_l &= \sum_n b_l^{(n)}(Q_1, Q_r) \cos 3\left(n + \frac{1}{2}\right)\varphi. \end{aligned} \tag{13}$$

In the following, we apply a first-order approximation for the functions $\mathcal{A}_{u/l}$ and $\mathcal{B}_{u/l}$

$$\begin{aligned} \mathcal{A}_u &\approx a_u^{(0)}(Q_1, Q_r) \cos\left(\tfrac{3}{2}\varphi\right), \\ \mathcal{A}_l &\approx a_l^{(0)}(Q_1, Q_r) \sin\left(\tfrac{3}{2}\varphi\right), \\ \mathcal{B}_u &\approx b_u^{(0)}(Q_1, Q_r) \sin\left(\tfrac{3}{2}\varphi\right), \\ \mathcal{B}_l &\approx b_l^{(0)}(Q_1, Q_r) \cos\left(\tfrac{3}{2}\varphi\right). \end{aligned} \tag{14}$$

This approximation is justified as follows: Lehner and Jungen [24] calculated the adiabatic-diabatic mixing angle $\beta_{2s,u/l}$ between ϕ_{2s} and $\phi_{u/l}$, which is related to $\mathcal{B}_{u/l}$ by

$$\mathcal{B}_{u/l} = \frac{\partial}{\partial \varphi} \beta_{2s,u/l}. \tag{15}$$

The variations of the angles $\beta_{2s,u/l}$ with respect to φ do not show any significant oscillations of an order higher than $\cos(\frac{3}{2}\varphi)$ [or $\sin(\frac{3}{2}\varphi)$], which is in agreement with our approximation of $\mathcal{B}_{u/l}$ in Eq. (14). Considering that the only difference between the functions $\mathcal{A}_{u/l}$ and $\mathcal{B}_{u/l}$ is the involved derivative, the approximation for $\mathcal{A}_{u/l}$ is also justified.

In addition to symmetry properties, another important feature is given by the fact that

$$\lim_{Q_r \to 0} \mathcal{B}_u = \lim_{Q_r \to 0} \mathcal{B}_l = 0, \tag{16}$$

which can be derived from symmetry arguments and was also shown numerically by Lehner and Jungen [24]. Apart from that, we can assume that the functions $\mathcal{A}_{u/l}$ and $\mathcal{B}_{u/l}$ neither show any other zeros nor vary dramatically in the region of the initial vibrational wave function. This assumption is backed by the numerical calculations of nonadiabatic couplings of Schneider and Orel [10] as well as Tashiro and Kato [2]. As a consequence, we approximate

$$a_u^{(0)}(Q_1, Q_r) \approx A_u, \tag{17}$$

$$a_l^{(0)}(Q_1, Q_r) \approx A_l, \tag{18}$$

$$b_u^{(0)}(Q_1, Q_r)/Q_r \approx B_u, \tag{19}$$

$$b_l^{(0)}(Q_1, Q_r)/Q_r \approx B_l, \tag{20}$$

where A_u, A_l, B_u, and B_l are constants. Using these simplifications, the nonadiabatic coupling operators read

$$\begin{aligned}\Lambda_{2s,u} &= A_u \cos(3\varphi/2)\frac{\partial}{\partial Q_r} + B_u \sin(3\varphi/2)\frac{1}{Q_r}\frac{\partial}{\partial\varphi},\\ \Lambda_{2s,l} &= A_l \sin(3\varphi/2)\frac{\partial}{\partial Q_r} + B_l \cos(3\varphi/2)\frac{1}{Q_r}\frac{\partial}{\partial\varphi}.\end{aligned} \tag{21}$$

III. QUASICLASSICAL PROPAGATION ON THE GROUND-STATE SURFACES

In our quasiclassical model, we simulate the propagation of wave functions, which correspond to the nonadiabatically transferred parts of the initial wave function. These parts are recognized in Eq. (7) as

$$\begin{aligned}d\chi_u &\equiv \Lambda_{2s,u}\chi_{2s}(t)dt,\\ d\chi_l &\equiv \Lambda_{2s,l}\chi_{2s}(t)dt,\end{aligned} \tag{22}$$

for the upper and lower ground states, respectively. The results for the coupling operators allow us to investigate how the functions $\chi_{2s}(t)$ are modified by the nonadiabatic coupling. In our model, the coupling for state $2sA_1'$ [Eq. (21)] includes the unknown parameters $A_{u/l}$ and $B_{u/l}$. As we are not interested in absolute predissociation rates, only the ratios $\delta_u = B_u/A_u$ and $\delta_l = B_l/A_l$ are of interest. Unless otherwise noted, the results presented in the following are obtained by using a trial value $\delta_{u/l} = 1$.

Although the ground states are populated in a continuous nonadiabatic transition from $2sA_1'$, it is sufficient to investigate the propagation of the transferred fractions given by Eq. (22). This may be justified as these fractions are subject to a monotonic propagation toward dissociation (ρ direction), without any reflections. Furthermore, the dissociation occurs faster than the phase modulation in $\chi_{2s}(t)$ [Eq. (5)]. Thus fractions transferred at different times are never subject to interferences and can be treated separately, regardless of their phase.

We represent the initial rovibrational wave functions χ_{2s} by linear combinations of basis states which are products of Wigner D functions and harmonic oscillator wave functions [29]

$$\begin{aligned}\chi_{2s} \equiv \chi^{N,v_1,v_2}_{K,M,l_2} = 1/\sqrt{2}\zeta^{v_1}(Q_1)\big[&\mathcal{D}^N_{KM}(a,b,c)\eta^{v_2,l_2}(Q_r,\varphi)\\ &+ u(-1)^N\mathcal{D}^N_{-KM}(a,b,c)\eta^{v_2,-l_2}(Q_r,\varphi)\big],\end{aligned} \tag{23}$$

where $\zeta^{v_1}(Q_1)$ corresponds to a one-dimensional harmonic oscillator wave function of the symmetric stretch mode while $\eta^{v_2,l_2}(Q_r,\varphi)$ represents the two-dimensional harmonic oscillator wave function of the degenerate modes. $\mathcal{D}^N_{KM}(a,b,c)$ denotes a Wigner D function depending on the Euler angles a, b, c. The parameter $u = \pm 1$ defines the symmetry of the wave function, which is A_1 for $u = 1$ and A_2 for $u = -1$. Other parameters in the functions $\zeta^{v_1}(Q_1)$ and $\eta^{v_2,l_2}(Q_r,\varphi)$ are chosen according to experimentally observed vibrational-level spacings and equilibrium positions [30–32]. In the experiments on three-body predissociation, the quantum number M is unknown, but uniformly distributed due to an isotropic environment. Therefore we assume a uniform statistical mixture of states with various values of the quantum number M.

A quasiphase-space distribution (QPD) for the vibrational coordinates $\mathbf{Q} = (Q_1, Q_{2a}, Q_{2b})$ is obtained by using the Wigner function

$$W_d(\mathbf{Q},\mathbf{P}) = \frac{1}{\pi}\int d^3\mathbf{s}\langle\mathbf{Q}-\mathbf{s}/2|\varrho|\mathbf{Q}+\mathbf{s}/2\rangle e^{-i\mathbf{P}\cdot\mathbf{s}}, \tag{24}$$

where the density matrix ϱ is given by

$$\varrho = \frac{1}{2N+1}\sum_{M=-N}^{N}\big|d\chi^{(M)}_{u/l}\big\rangle\big\langle d\chi^{(M)}_{u/l}\big|. \tag{25}$$

The M dependency of $\chi^{(M)}_{u/l}$ can be seen from Eqs. (22) and (23).

Substantial test calculations revealed that centrifugal distortions due to rotations in the Euler angles a and b are negligible. Hence the angles a and b were kept fixed in the classical propagation. The initial rotation in the Euler angle c is given by the quantum number K. The simulations were tested for several choices of K. For low rotational excitations ($K \leqslant 3$), which are typical for the experimental data [3], observed variations of the results were marginal. This is in agreement with the results from Lehner and Jungen [24]. Therefore, K was chosen according to the most typical value in the experiment, in consideration of the restrictions given by the rovibronic symmetry.

To account for energy conservation, we restrict the QPD in energy space to $W \pm 0.2$ eV, where W is the total energy of the initial state. The QPD is propagated by a CTMC method. In the present model we restrict the propagation to a single surface (upper or lower), which means that the nonadiabatic coupling between the two ground-state surfaces is neglected. The consequences of this restriction will be discussed in the next section.

The data for the potential surfaces were obtained by Jungen [3]. It extends to a separation distance of the nuclei which corresponds to a hyperradius $\rho = 8.9$ a.u. At this value the mutual interaction of nuclei has virtually ceased for the upper sheet, hence the momentum distributions obtained at this value correspond to the final distributions. The distribution of momentum configurations resulting from the propagation on the upper sheet are derived according to Eqs. (A9) and (A14) in the Appendix. The momentum configuration distributions are displayed in Dalitz plots. Figure 1 shows the configuration geometries which are mapped in a Dalitz plot, while the definition of its coordinates is described in the Appendix.

In contrast to the upper sheet, for large values of ρ the lower sheet is governed by attractive two-particle interactions, which enable two-body decay ($H + H_2$). At $\rho = 8.9$ a.u., the internal energy of the two closest nuclei is calculated for each trajectory. If this energy is positive, the trajectory results in three-body decay, otherwise in two-body decay. The three-body momentum configurations obtained at this separation distance are less reliable than those obtained on the upper sheet because many trajectories are still influenced by the attractive two-particle interactions.

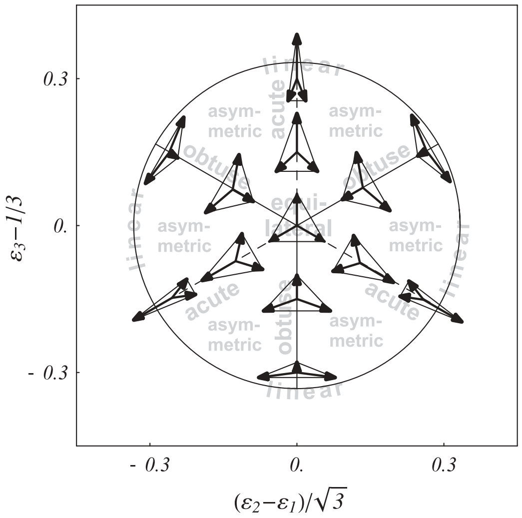

FIG. 1. Allocation of momentum configurations in a Dalitz plot. The plot coordinates are explained in Eq. (A14).

IV. RESULTS AND DISCUSSION

Table II shows the fraction of trajectories leading to three-body dissociation after direct coupling to the lower ground state. For the investigated levels of $2sA_1'$, this fraction varies from $\approx 1\%$ [$D_3(v_1 = 0, v_2 = 0)$] to $\approx 6\%$ [$H_3(v_1 = 2, v_2 = 1)$]. In general, the fraction of three-body dissociations increases for higher vibrational excitations, while for H_3 the fractions are higher than the corresponding results for D_3.

The direct population of the lower ground state by nonadiabatic transitions from the $2sA_1'$ states is significantly weaker than for the upper ground state [2]. In consideration of the low fractions of three-body decay in this process, we can conclude that three-body decay resulting from direct coupling to the lower ground state is negligible in comparison to three-body decay resulting from direct coupling to the upper ground state, as long as couplings among the two ground states are not taken into account.

In fact, the Jahn-Teller-type coupling among the two ground states is very strong in the vicinity of the conical intersection at equilateral geometries. For nuclear wave functions which have significant amplitudes at this configuration the coupling results in a population transfer between the adiabatic states. Mahapatra and Köppel [25] showed that for Gaussian wave packets initially located at the seam of the conical intersection the transfer predominantly proceeds from the upper state to the lower state. However, after 15 fs, when the molecule is practically dissociated, still $\approx$20% of the initial upper-state population remains in the upper state. Our calculations for the upper state describe the propagation of the part which is not transferred to the lower state. In view of our results for the lower state, we can expect that most of the population which is transferred to the lower state will result in two-body dissociations. Small contributions of three-body decay resulting from dissociation via the lower state (either arising from direct transitions from $2sA_1'$ or from transitions from the upper state) are not included in the final state distributions derived here.

TABLE II. Fractions of three-body dissociation after direct coupling to the lower ground state.

H_3			
$2sA_1'$	$v_1 = 0$	$v_1 = 1$	$v_1 = 2$
$v_2 = 0$	0.022	0.032	0.039
$v_2 = 1$	0.029	0.045	0.061
D_3			
$2sA_1'$	$v_1 = 0$	$v_1 = 1$	$v_1 = 2$
$v_2 = 0$	0.010	0.024	0.024
$v_2 = 1$	0.014	0.033	0.039

Figure 2 shows Dalitz plots which present momentum configurations obtained for predissociation of vibrational levels of $2sA_1'$ via the upper ground-state sheet. The degenerate mode quantum number v_2 is kept zero while the stretching mode quantum number v_1 is varied from 0 to 2 for both H_3 and D_3. The rotational quantum number K was set to zero.

Despite the absence of Jahn-Teller-type coupling in our model, our results are in good qualitative agreement with the experiments (first row of Figs. 7 and 9 in Ref. [3]). In particular, we reproduce several key features of the data: First, there are three dominant maxima at geometries which correspond to obtuse-angled triangles in momentum space. The maxima are also similar with respect to their width. Second, configurations with low density can be found in the central region (near equilateral geometries) and at near-linear geometries close to the edge of the circular plot region, located in between the three maxima. And third, for increasing excitation of the symmetric stretch mode the correlation structure appears to contract slightly toward the center of the plot. Missing features of the theoretical results can be identified as the absence of the clear zero in the center as well as the wings of faint intensity at acute-angled near-linear geometries. Also in contrast to the experiment, the plots for $v_1 = 1$ and $v_1 = 2$ show a weak local maximum in the center, which is slightly stronger for H_3 in comparison to D_3. Other isotope effects are very weak.

Figure 3 shows as an example the temporal evolution of spatial configurations for the dissociation of $2sA_1'(1,0)$ of H_3. Note that here we use polar plots of the hyperspherical coordinates (ϑ, φ) (see Appendix), which is equivalent to a Dalitz plot for spatial coordinates. The $t = 0$ plot shows the density of the initial starting points, which were randomly generated according to the Wigner distribution [Eq. (24)]. The pattern of this density results from properties of the nonadiabatic coupling, as well as the initial vibrational wave function. In these coordinates, the density of a $v_2 = 0$ vibrational wave function is just a symmetrical Gaussian centered at the origin. After a nonadiabatic transition to the upper ground state, this wave function is transformed according to Eq. (22), where $\Lambda_{2s,u}$ is given by Eq. (21). For $v_2 = 0$, the vibrational wave function is independent of φ, hence the second term of $\Lambda_{2s,u}$ (containing $\partial/\partial\varphi$) does not contribute. The pattern at $t = 0$ is therefore a direct consequence of the two factors in the first term of $\Lambda_{2s,u}$: The factor $\cos(3/2\varphi)$ generates node lines at acute-angled geometries (compare Fig. 6, lower part) and maxima at obtuse-angled geometries. The operator $\partial/\partial Q_r$ gives rise to a zero in the center.

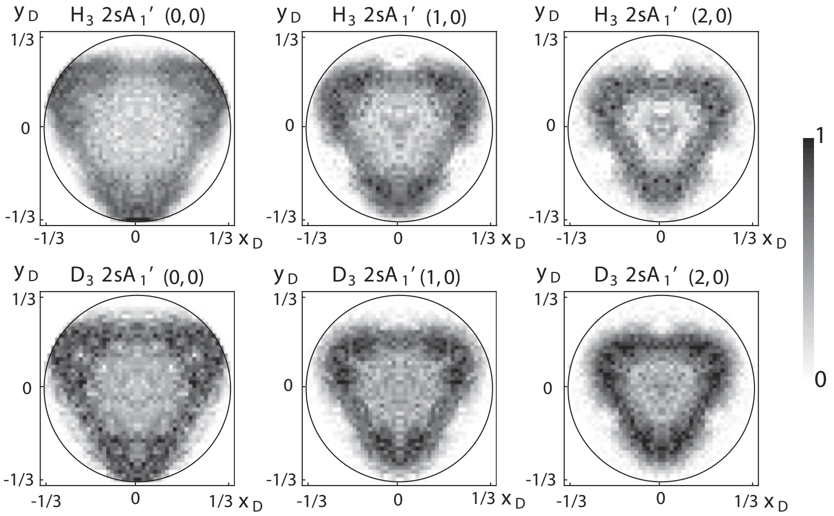

FIG. 2. Momentum configuration maps obtained from the simulation of $2sA_1'(v_1, v_2 = 0)$, $K = 0$ states of D_3 and H_3. The calculations were carried out on the upper ground state. The coordinates x_D and y_D are defined by Eq. (A14) in the Appendix. See Fig. 1 for an illustration of the associated configurations.

It might seem that this initial pattern is retained in the final momentum configuration. However, what precisely happens during the propagation on the upper sheet is shown in the plots for $t > 0$ in Fig. 3: At $t = 100$ a.u. as well as at $t = 200$ a.u., the density is transformed to a pattern which now features maxima at acute-angled geometries. For $t \geqslant 300$ a.u. the pattern again shows maxima at obtuse-angled geometries, though the node lines between these maxima appear increasingly washed out. A more detailed examination of the evolution of the density reveals an oscillatory motion by which the pattern first contracts toward the center, then expands again in an inverted (acute-angled) configuration, followed by another contraction, and another inversion to obtuse-angled geometries. These dynamics are a direct consequence of the steep cone of the upper potential sheet, which is centered at the conical intersection with the lower sheet at $\vartheta = 90^\circ$. This motion in the coordinates (ϑ, φ) is accompanied by a continuously increasing hyperradius ρ, which is the consequence of initial momenta in the ρ direction.

For increasing ρ, the slope of the cone of the upper sheet decreases continuously, as the atoms separate spatially and the mutual interaction is reduced. For this reason, the oscillatory motion in the coordinates (ϑ, φ) abates after one cycle and the spatial as well as the momentum configuration distributions remain in a pattern which features maxima at obtuse-angled geometries, as seen in the final momentum configurations.

The contraction of the momentum configuration structures for increasing excitation of the stretching mode observed in the plots in Fig. 2 is not surprising: The higher the excitation of the stretching mode, the higher is the average momentum toward dissociation (ρ direction). A larger share of momentum in this direction leads to a shift toward the equilateral triangle configuration in momentum space, which is retained during the propagation and thus observed in the final-state distribution.

It is not surprising that the zero observed in the center of the experimental plots is not strictly reproduced in this model. Trajectories which end up in these equilateral final configurations linger for a long time in configurations which are subject to strong Jahn-Teller-type couplings, hence their contributions are not reliable. The experimentally observed features at almost-linear acute-angled geometries are most likely contributions from three-body dissociation on the lower ground-state surface, which was populated by direct coupling from $2sA_1'$ or by Jahn-Teller-type coupling.

Figure 4 shows final momentum distributions which result from simulations of dissociation of degenerate-mode excited

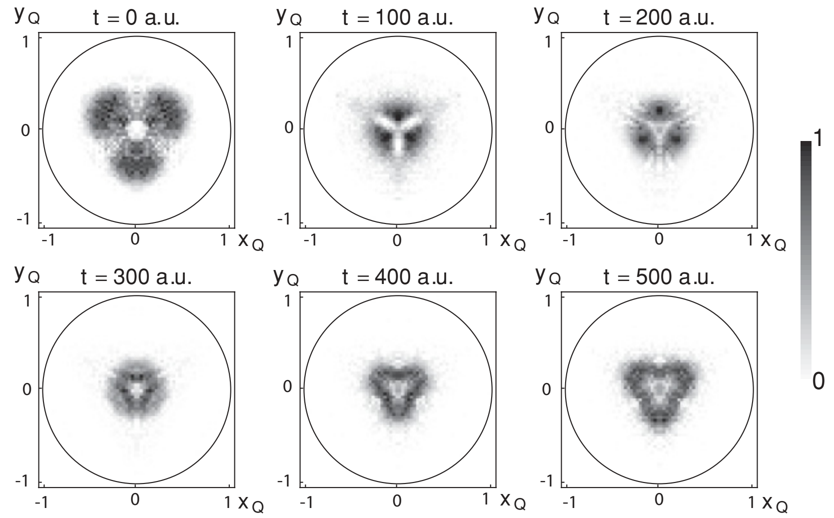

FIG. 3. Evolution of spatial configurations during the propagation on the upper sheet. The coordinates are given by $x_Q = \cos\vartheta \sin\varphi$, $y_Q = \cos\vartheta \cos\varphi$ (see Fig. 6, right part). This example corresponds to the state $2sA_1'(1, 0)$ of H_3.

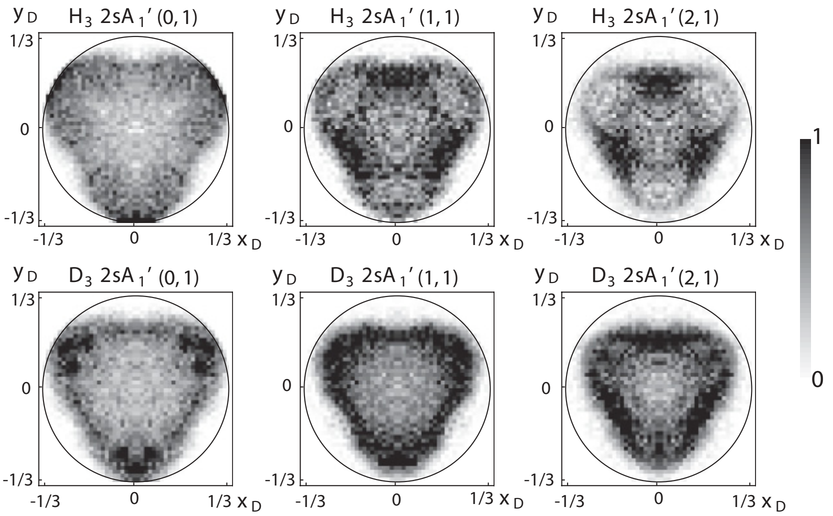

FIG. 4. Momentum configuration maps obtained from simulation of $2sA_1'(v_1, v_2 = 1)$, $K = 2$ states of D$_3$ and H$_3$ using $\delta_u = 1$. The calculations were carried out on the upper ground state.

vibrational levels ($v_2 = 1$) of $2sA_1'$. For the rotational quantum number, we chose $K = 2$ to reproduce the states investigated in the experiment [33]. In contrast to the preceding examples, the initial vibrational wave functions used for these simulations are no longer independent of φ, meaning that now both terms of $\Lambda_{2s,u}$ in Eq. (21) contribute. The relative weight of the two terms is controlled by the parameter δ_u. As the exact value of δ_u is unknown, results are shown for two reasonable choices, $\delta_u = 1$ and $\delta_u = 3$.

Figure 4 shows results for $\delta_u = 1$. On first sight, features which were recognized for plots with $v_2 = 0$ can also be found in the plots for $v_2 = 1$: Again some of the plots show three maxima at obtuse-angled geometries, similar to the striking maxima which appear for $v_2 = 0$. These maxima are most prominent for $v_1 = 0$ and become weaker for higher v_1. They also appear slightly stronger for D$_3$ in comparison to H$_3$. Another feature which is recognized is that again no significant density appears beyond the triangular area spanned by these three maxima (at acute-angled almost-linear geometries). Again the area of significant density seems to shrink for higher excitations of the stretching mode ($v_1 = 1, 2$).

A clear difference to the plots for $v_2 = 0$ can be found in three additional maxima at acute-angled geometries, which appear in the plots for H$_3$, (1, 1) and (2, 1) as well as D$_3$, (2, 1). In view of the formation process of the obtuse-angled structure, which was described earlier, this additional feature can be attributed to the additional second term in the expression for $\Lambda_{2s,u}$: The factor $\sin 3/2\varphi$ appearing in this term gives rise to contributions at acute-angled geometries in the spatial density at $t = 0$, which are propagated by the aforementioned oscillatory motion to a corresponding pattern in the final-state distribution. In the simulations for $\delta_u = 1$, the feature at acute-angled geometries does not appear for lower values of v_1 because in these cases a large part of the corresponding regions of phase space are not in agreement with the total energy of the system and hence are sorted out before the propagation is started.

The connection between the two terms in $\Lambda_{2s,u}$ and the obtuse-angled or acute-angled structures can be demonstrated by changing the parameter δ_u. Figure 5 shows plots for the same states as in Fig. 4, calculated for $\delta_u = 3$. Using this value, the second term of $\Lambda_{2s,u}$ (containing $\sin 3/2\varphi$) has stronger weight in comparison to the first term (containing $\cos 3/2\varphi$). At first sight, this variation of δ_u does not seem to cause strong changes in the overall structure. On closer examination, however, it appears that regions of acute-angled geometries

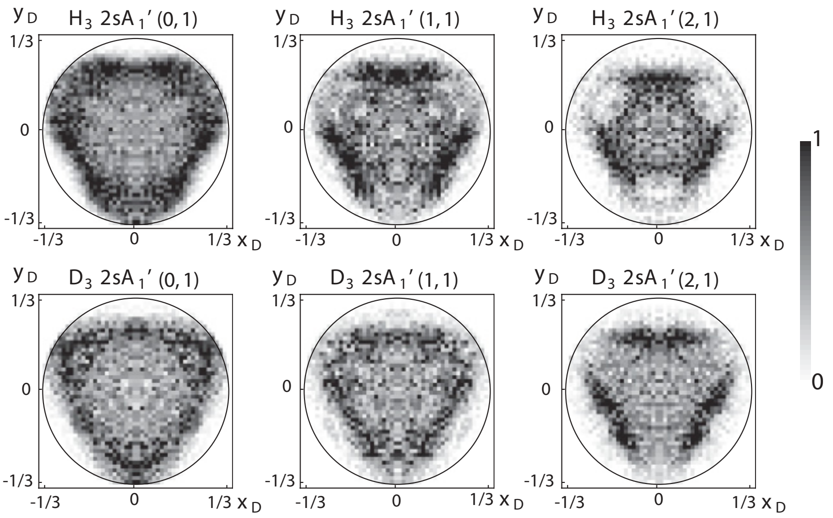

FIG. 5. Momentum configuration maps obtained from the simulation of $2sA_1'(v_1, v_2 = 1)$, $K = 2$ states of D$_3$ and H$_3$ using $\delta_u = 3$. The calculations were carried out on the upper ground state.

gained intensity in comparison to regions of obtuse-angled geometries. This is most obvious in the plots for $v_1 = 0$ of H_3, where the highest densities are no longer found at almost-linear obtuse-angled configurations (for $\delta_u = 1$), but in the form of three elongate bands at acute-angled geometries (for $\delta_u = 3$).

Experimental plots which correspond to $2sA_1'(v_2 = 1)$ also feature maxima at obtuse-angled geometries as well as acute-angled geometries (see second row of Figs. 7 and 9 in Ref. [3]). Their location corresponds to the location of the maxima seen in the simulations: The "acute" maxima appear closer to the center than the "obtuse" maxima, giving the impression of a triangle formed by the "obtuse" maxima at the corners and the "acute" maxima on the connecting lines. The experimental plot for D_3 ($v_1 = 0$) is an exception because here "obtuse" maxima are comparatively weak (eventually stronger maxima will appear at near-linear geometries, which were not accessible experimentally).

In contrast to the theoretical results, the experimental plots also show a clear maximum at the center. This deficiency can again be attributed to the absence of Jahn-Teller coupling in our model: In contrast to the states with $v_2 = 0$, the nonadiabatically transferred parts $d\chi_u$ and $d\chi_l$ do not vanish at equilateral geometries for $v_2 = 1$. This results in a strong population exchange between upper and lower states (both directions), which is not included in our model. It is likely that a certain part of the nuclear wave function remains in the equilateral configuration, populating both upper and lower electronic states, or in an alternative picture, a diabatic state. This part finally results in the contributions observed at the center of the experimental plots.

It can be concluded from the comparison between experiment and theory that, in principle, our model is capable of reproducing the structures at obtuse-angled and acute-angled geometries, although the relative weighting of both kinds of structures is incorrect. To some degree this weighting is influenced by the parameter δ_u. For optimal agreement with the experiment, however, it would be necessary to adjust the relative weighting for each value of v_2 independently. Adjusting the parameter δ_u like that is unreasonable because δ_u is by definition independent from vibrational quantum numbers. A possible conclusion is that trajectories which originate from the two terms of $\Lambda_{2s,u}$ are subject to varying probabilities for transitions to the lower ground state and are thus depleted from the upper state in unequal proportion.

V. CONCLUSION

We show that many of the momentum configuration structures observed in predissociation of $2sA_1'$ can be interpreted and reproduced by a simple model for the nonadiabatic coupling. This model is derived from symmetry considerations. It is shown that the final momentum distributions are directly related to the essential geometrical properties of the nonadiabatic coupling and the initial vibrational wave function. These properties favor certain obtuse-angled breakup geometries in the case of vibrational states with $v_2 = 0$, while allowing obtuse *and* acute-angled geometries for states with $v_2 = 1$. The dynamics which transform patterns imprinted by the coupling to the final-state distributions are identified as an oscillatory motion on the upper ground-state sheet, which is induced by its conical structure at short nuclear distances.

It is an important insight that the formation of the basic patterns in the final momentum configuration already occurs in the nonadiabatic transition from $2sA_1'$ to the upper ground state, while the effect of the dynamics on the coupled ground-state surfaces can be regarded as a slight deformation and selective filtering. A major part of the dynamics which result in three-body decay seems to proceed on the upper adiabatic ground-state sheet only. Apparently, one effect of the lower ground state and the Jahn-Teller-type coupling is to selectively depopulate the upper state. A few experimental observations give hints for three-body dissociation via the lower adiabatic ground state (structures at acute-angled, near-linear geometries) or dissociation by strongly Jahn-Teller coupled (diabatic) states (structures at equilateral geometries).

Our results for levels with $v_2 = 0$ are in agreement with those of Lehner and Jungen. For the $v_2 = 1$ levels, however, clear differences are apparent. Here the results of Lehner and Jungen showed typically strong contributions at acute angled geometries and weak contributions at obtuse-angled geometries. This difference can be attributed to the fact that Lehner and Jungen did not account for the derivative coupling which involves Q_r (or related coordinates).

The ultimate aim of this work is to enhance the general understanding of predissociation mechanisms in H_3 and related molecules. More sophisticated efforts which contribute to the interpretation of the huge amount of momentum correlation structures of other states of H_3 and D_3 are welcomed.

ACKNOWLEDGMENTS

I kindly thank Prof. M. Jungen for providing me his data on the ground potential surfaces, which was indispensable for this work. Special thanks go to Dr. B. Lepetit as well as Prof. J. M. Rost for their cordial support and fruitful discussions. In its initial stage this work was funded by DFG Project No. He2525-1.

APPENDIX: SPATIAL AND MOMENTUM COORDINATES FOR THREE IDENTICAL PARTICLES

This Appendix provides definitions for the various sets of momentum and position coordinates used in this article.

1. Hyperspherical coordinates

The set of hyperspherical coordinates $(\rho, \vartheta, \varphi)$ we use in Fig. 3 is the same as in Ref. [3]. It is defined by its relation to mass-scaled Jacobi vectors $\mathbf{r}$ and $\mathbf{R}$

$$\begin{aligned} v_1 &= |\mathbf{r}|^2 - |\mathbf{R}|^2 = \rho^2 \cos\vartheta \cos\varphi, \\ v_2 &= 2\mathbf{r} \cdot \mathbf{R} = \rho^2 \cos\vartheta \sin\varphi, \\ v_3 &= 2|\mathbf{r} \times \mathbf{R}| = \rho^2 \sin\vartheta, \end{aligned} \tag{A1}$$

where (v_1, v_2, v_3) can be interpreted as Cartesian coordinates of configuration space. A one-to-one mapping of this vector space to three-particle configurations is provided if $v_3 \geqslant 0$, which implies $0 \leqslant \vartheta \leqslant \pi/2$ and $0 \leqslant \varphi \leqslant 2\pi$. The relation to row-orthonormal hyperspherical coordinates $(\rho_K, \theta_K, \delta_K)$

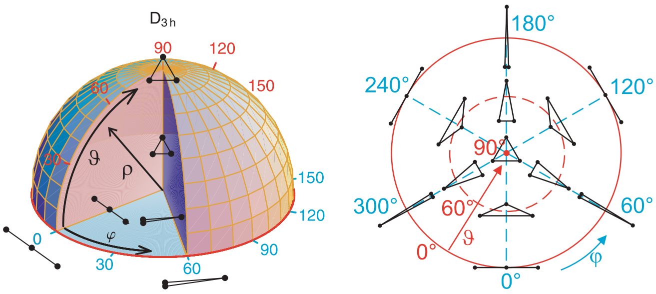

FIG. 6. (Color online) Configurations associated with hyperspherical coordinates. Left: Nuclear configurations on a sphere described by hyperspherical coordinates. Right: Configurations for a fixed value of ρ; the presentation corresponds to the view from above on the sphere on the left.

defined by Kuppermann [34] is given by

$$\begin{aligned} \rho &= \rho_K, \\ \vartheta &= 2\theta_K, \\ \varphi &= 2\pi - 2\delta_K. \end{aligned} \tag{A2}$$

Figure 6 indicates schematically the configurations assigned to our hyperspherical coordinates. The angles ϑ and φ correspond to spherical latitudes and longitudes and describe the shape of the triangle that is formed by the three particles. The hyperradius ρ solely defines the overall size of the triangle and leaves the internal angles unchanged. The value $\vartheta = 0^\circ$ always corresponds to linear arrangements, $\vartheta = 90^\circ$ always corresponds to the equilateral triangle. For $\varphi = n \times 60^\circ$, where n is integer, the shape is always isosceles, either acute (n odd) or obtuse (n even).

Our internal coordinates refer to the Eckart frame, which is in contrast to Kuppermann's definition, which is based on the principal axis frame.

2. Hyperspherical coordinates for normal coordinate space

An X_3 molecule which forms an equilateral triangle in its equilibrium geometry features three vibrational normal modes: The symmetric stretch mode, Q_1, and two degenerate modes, Q_{2a} and Q_{2b}.

The relation to the spatial coordinates (x_i, y_i) of nucleus i in the Eckart frame is given by

$$\begin{pmatrix} x_i \\ y_i \end{pmatrix} = \frac{1}{\sqrt{m}} \mathbf{l}_i \mathbf{Q} + \mathbf{r}_i^0, \tag{A3}$$

where m is the proton mass, $\mathbf{r}_i^0$ the equilibrium position of nucleus i, and $\mathbf{Q} = (Q_1, Q_{2a}, Q_{2b})$. The matrices l_i are given by

$$\begin{aligned} \mathbf{l}_1 &= \frac{1}{\sqrt{3}} \begin{pmatrix} 1 & -1 & 0 \\ 0 & 0 & 1 \end{pmatrix}, \\ \mathbf{l}_2 &= \frac{1}{\sqrt{3}} \begin{pmatrix} -1/2 & 1/2 & -\sqrt{3}/2 \\ -\sqrt{3}/2 & -\sqrt{3}/2 & -1/2 \end{pmatrix}, \\ \mathbf{l}_3 &= \frac{1}{\sqrt{3}} \begin{pmatrix} -1/2 & 1/2 & \sqrt{3}/2 \\ \sqrt{3}/2 & \sqrt{3}/2 & -1/2 \end{pmatrix}, \end{aligned} \tag{A4}$$

and

$$r_1^0 = r_e \begin{pmatrix} 1 \\ 0 \end{pmatrix}, \quad r_2^0 = r_e \begin{pmatrix} -1/2 \\ -\sqrt{3}/2 \end{pmatrix}, \quad r_3^0 = r_e \begin{pmatrix} -1/2 \\ \sqrt{3}/2 \end{pmatrix}, \tag{A5}$$

where r_e is the equilibrium distance of the nuclei.

Alternative coordinates for the degenerate modes are

$$Q_r^2 = Q_{2a}^2 + Q_{2b}^2 \quad \text{and} \quad \varphi = \arctan(Q_{2b}/Q_{2a}), \tag{A6}$$

where φ is identical to the hyperspherical angle.

The vibrational levels are labeled by the quantum numbers (v_1, v_2), where v_1 refers to excitations of the symmetric stretch mode and v_2 to excitations in the degenerate modes. Basis states of the degenerate modes are usually labeled by the vibrational angular momentum quantum number $l = \{-v_2, -v_2 + 2, \dots, v_2 - 2, v_2\}$.

Normal coordinates are related to hyperspherical coordinates as follows

$$\begin{aligned} \tilde{Q}_1 &= \sqrt{m} 3^{-1/4} \rho \sin \tilde{\vartheta}, \\ Q_{2a} &= 3^{-1/4} \sqrt{m} \rho \cos \varphi \cos \tilde{\vartheta}, \\ Q_{2b} &= 3^{-1/4} \sqrt{m} \rho \sin \varphi \cos \tilde{\vartheta}, \\ Q_r &= 3^{-1/4} \sqrt{m} \rho \cos \tilde{\vartheta}. \end{aligned} \tag{A7}$$

Here, the substitutions $\tilde{Q}_1 = Q_1 + \sqrt{m} r_e$ and $\tilde{\vartheta} = \vartheta/2 + \pi/4$ were used (r_e being the equilibrium distance between two nuclei). Equation (A7) shows that the set of hyperspherical coordinates $(\rho, \tilde{\vartheta}, \varphi)$ describes configurations in the space which is spanned by the Cartesian coordinates $(\tilde{Q}_1, Q_{2a}, Q_{2b})$. In this space, the $(\tilde{Q}_1 = 0)$ plane as well as the $\tilde{Q}_1$ axis correspond to the equilateral triangle. Linear configurations are found on the two cones which correspond to $\tilde{\vartheta} = \pm\pi/4$. The half-sphere shown in Fig. 6 is mapped onto the area confined by $\pi/4 \leqslant \tilde{\vartheta} \leqslant \pi/2$. This restriction provides a one-to-one mapping to configuration space.

3. Momentum coordinates and Dalitz plots

So far the coordinates introduced were all describing spatial configurations. In the following similar coordinates will be defined for momentum space. Let $\mathbf{P}_i = (p_{x_i}, p_{y_i})$ be the momentum coordinates of particle i in the center-of-mass frame (w.l.o.g. $p_{z_i} = 0$). Now we introduce hyperspherical momentum coordinates analog to Eq. (A1). Therefore we first define "Jacobi coordinates" for momenta

$$\begin{aligned} \mathbf{r}_p &= \frac{\sqrt{2}}{3^{1/4}} (\mathbf{P}_1 - \mathbf{P}_2), \\ \mathbf{R}_p &= \frac{3^{1/4}}{\sqrt{2}} [\mathbf{P}_3 - (\mathbf{P}_1 + \mathbf{P}_2)]. \end{aligned} \tag{A8}$$

And we adopt the framework from Eq. (A1)

$$\begin{aligned} w_1 &= |\mathbf{r}_p|^2 - |\mathbf{R}_p|^2 = \rho_p^2 \cos \vartheta_p \cos \varphi_p, \\ w_2 &= 2\mathbf{r}_p \cdot \mathbf{R}_p = \rho_p^2 \cos \vartheta_p \sin \varphi_p, \\ w_3 &= 2|\mathbf{r}_p \times \mathbf{R}_p| = \rho_p^2 \sin \vartheta_p. \end{aligned} \tag{A9}$$

It follows directly from the definitions (A8) and (A9)

$$\rho_p^2 = \sqrt{w_1^2 + w_2^2 + w_3^2} = 2\sqrt{3}mT, \tag{A10}$$

where T is the total kinetic energy of the system. We can also introduce normal momenta coordinates by an equation analogous to Eq. (A7)

$$\begin{aligned} P_1 &= 3^{-1/4}\sqrt{m}^{-1}\rho_P \sin\tilde{\vartheta}_P, \\ P_{2a} &= 3^{-1/4}\sqrt{m}^{-1}\rho_P \cos\varphi_P \cos\tilde{\vartheta}_P, \\ P_{2b} &= 3^{-1/4}\sqrt{m}^{-1}\rho_P \sin\varphi \cos\tilde{\vartheta}_P, \end{aligned} \tag{A11}$$

where again $\tilde{\vartheta}_P = \vartheta_P/2 + \pi/4$. Now the total kinetic energy can be expressed as

$$T = \tfrac{1}{2}\left(P_1^2 + P_{2a}^2 + P_{2b}^2\right). \tag{A12}$$

Note that (P_1, P_{2a}, P_{2b}) are different from the classical canonical momentums $(P_1^c = \dot{Q}_1, P_{2a}^c = \dot{Q}_{2a}, P_{2b}^c = \dot{Q}_{2b})$. They only coincide if the system is not rotating.

As a particularly interesting result we find that the coordinates (w_1, w_2) can be written in terms of the kinetic energies of the particles $E_i = |\mathbf{P}_i|^2/(2m)$

$$\begin{aligned} w_1 &= -2 \times 3^{3/2}m(E_3 - \tfrac{1}{3}T), \\ w_2 &= 6m(E_2 - E_1). \end{aligned} \tag{A13}$$

If the total kinetic energy is not of interest, the coordinates

$$\begin{aligned} x_D &\equiv w_2/(-2 \times 3^{3/2}mT) = (\varepsilon_2 - \varepsilon_1)/\sqrt{3}, \\ y_D &\equiv w_1/(-2 \times 3^{3/2}mT) = \varepsilon_3 - 1/3, \end{aligned} \tag{A14}$$

where $\varepsilon_i = E_i/T$ describe the configuration space of the relative arrangements of momentum vectors. (x_D, y_D) are also known as the coordinates of the Dalitz plot, which is frequently used to display momentum configurations in three-body dissociations [3,4,16].

This shows how the coordinates of the Dalitz plot are related to hyperspherical coordinates: If we define hyperspherical coordinates for momenta as described in Eqs. (A8) and (A9), then a sphere in this coordinate space corresponds to a surface of constant total kinetic energy. If we normalize the radius of this sphere to $1/3$ and project it onto the equator plane, we get the configuration space of the Dalitz plot (see also Appendix in Ref. [3]). Because of this analogy, the lower part of Fig. 6 can also be understood as showing momentum configurations in the Dalitz plot.

---

[1] V. Kokoouline and C. H. Greene, Phys. Rev. A **68**, 012703 (2003).

[2] M. Tashiro and S. Kato, J. Chem. Phys. **117**, 2053 (2002).

[3] U. Galster, F. Baumgartner, U. Müller, H. Helm, and M. Jungen, Phys. Rev. A **72**, 062506 (2005).

[4] C. M. Laperle, J. E. Mann, T. G. Clements, and R. E. Continetti, Phys. Rev. Lett. **93**, 153202 (2004).

[5] P. C. Cosby and H. Helm, Phys. Rev. Lett. **61**, 298 (1988).

[6] J. Peterson, P. Devynck, C. Hertzler, and W. Graham, J. Chem. Phys. **96**, 8128 (1992).

[7] C. Bordas and H. Helm, Phys. Rev. A **47**, 1209 (1993).

[8] U. Müller and P. C. Cosby, J. Chem. Phys. **105**, 3532 (1996).

[9] U. Müller and P. C. Cosby, Phys. Rev. A **59**, 3632 (1999).

[10] I. Schneider and A. Orel, J. Chem. Phys. **111**, 5873 (1999).

[11] I. Mistrík, R. Reichle, U. Müller, H. Helm, M. Jungen, and J. A. Stephens, Phys. Rev. A **61**, 033410 (2000).

[12] F. Baumgartner and H. Helm, Phys. Rev. Lett. **104**, 103002 (2010).

[13] I. F. Schneider, A. Orel, and A. Suzor-Weiner, Phys. Rev. Lett. **85**, 3785 (2000).

[14] V. Kokoouline, C. H. Greene, and B. D. Esry, Nature (London) **412**, 891 (2001).

[15] A. Suzor-Weiner and I. F. Schneider, Nature (London) **412**, 871 (2001).

[16] D. Strasser, L. Lammich, H. Kreckel, S. Krohn, M. Lange, A. Naaman, D. Schwalm, A. Wolf, and D. Zajfman, Phys. Rev. A **66**, 032719 (2002).

[17] B. McCall *et al.*, Nature (London) **422**, 500 (2003).

[18] M. Larsson, B. McCall, and A. Orel, Chem. Phys. Lett. **462**, 145 (2007).

[19] J. Blandon and V. Kokoouline, Phys. Rev. Lett. **102**, 143002 (2009).

[20] I. Dabrowski and G. Herzberg, Can. J. Phys. **58**, 1238 (1980).

[21] C. Bordas, P. C. Cosby, and H. Helm, J. Chem. Phys. **93**, 6303 (1990).

[22] I. Mistrík, R. Reichle, H. Helm, and U. Müller, Phys. Rev. A **63**, 042711 (2001).

[23] B. Lepetit, R. Abrol, and A. Kuppermann, Phy. Rev. A **76**, 040702(R) (2007).

[24] M. Lehner and M. Jungen, J. Phys. B **42**, 065101 (2009).

[25] S. Mahapatra and H. Köppel, J. Chem. Phys. **109**, 1721 (1998).

[26] M. Hamermesh, *Group Theory And Its Application To Physical Problems* (Addison-Wesley, Reading, MA, 1962).

[27] S. Althorpe, J. Chem. Phys. **124**, 084105 (2006).

[28] H.-G. Yu, Chem. Phys. Lett. **281**, 312 (1997).

[29] F. Karlický, B. Lepetit, R. Kalus, and F. Gadéa, J. Chem. Phys. **126**, 174305 (2007).

[30] H. Figger, W. Ketterle, and H. Walther, Z. Phys. D **13**, 129 (1989).

[31] W. Ketterle, H.-P. Messmer, and H. Walther, Europhys. Lett. **8**, 333 (1989).

[32] U. Müller, M. Braun, R. Reichle, and R. Salzgeber, J. Chem. Phys. **108**, 4478 (1998).

[33] U. Galster, Ph.D. thesis, Physikalisches Institut, Universität Freiburg, Germany (2006).

[34] A. Kuppermann, J. Phys. Chem. **100**, 2621 (1996).